Biomagnetics

Study on Worst-Case Gradient Forces on Untethered Magnetic Devices Using Two Synchronized Rotating Magnetic Dipoles

Zhengya Zhang[1,2,3], Bohuan Lin[4], Anke Klingner[5], Guang Feng[2], Yanfei Liao[6], Jian Guo[6], Wei Xue[2], Fengping Li[2], Wujun Geng[2], Sarthak Misra[3,7*], and Islam S.M.Khalil[8**]

[1] *School of Robot Engineering, Wenzhou University of Technology, Wenzhou 325000, China*
[2] *Oujiang Laboratory (Zhejiang Lab for Regenerative Medicine, Vision and Brain Health), Wenzhou 325000, China*
[3] *Surgical Robotics Laboratory, Department of Biomaterials and Biomedical Technology, University of Groningen and University Medical Center Groningen, 9713 AV Groningen, The Netherlands*
[4] *Department of Foundational Mathematics, Xi'an Jiaotong Liverpool University, Suzhou 215123, China*
[5] *Department of Physics, The German University in Cairo, Cairo 11835, Egypt*
[6] *College of Mechanical and Electrical Engineering, Wenzhou University, Wenzhou 325000, China*
[7] *Surgical Robotics Laboratory, Department of Biomechanical Engineering, University of Twente, 7500 AE Enschede, The Netherlands*
[8] *Robotics and Mechatronics Research Group, University of Twente, 7500 AE Enschede, The Netherlands*
[*] *Senior Member, IEEE*
[**] *Member, IEEE*

Received 7 Dec 2025, revised 3 Jan 2026, accepted 11 Jan 2026, published 23 Jan 2026, current version 19 Feb 2026.

Abstract—Untethered magnetic devices (UMDs) hold significant clinical potential for removing blood clots. However, in the complex intravascular environment, their locomotion may be disturbed. Such disturbances can lead to variations in the magnetic gradient force exerted on the UMD, increasing the risk of vascular damage. Therefore, evaluating the magnetic gradient force acting on the UMD under worst-case conditions is essential for risk mitigation. In this letter, we a novel method to estimate the upper and lower bounds of the worst-case magnetic gradient force acting on the UMD, with actuation provided by two synchronized rotating magnetic dipoles. To assess the robustness of the algorithm, we conducted a Monte Carlo simulation in which the dipole directions of the two synchronized rotating magnetic dipoles and the dipole direction of the UMD were randomly varied 1 000 000 times in the three-dimensional space to simulate all possible scenarios that may be encountered by the UMD in intravascular environments. The simulation results indicate that the worst-case magnetic gradient force remains below the upper bound predicted by the algorithm, thereby validating its effectiveness.

Index Terms—Biomagnetics, magnetic gradient force, Monte Carlo simulation, untethered magnetic devices, worst-case conditions.

I. INTRODUCTION

Untethered magnetic devices (**UMDs**) represent a promising minimally invasive approach for clearing blood clots within vascular environments [Khalil 2019, Song 2024]. However, the complex rheological environment of blood imposes substantial challenges to the control of their locomotion [Bishop 2001]. The aggregation of red blood cells and the localized accumulation of platelets may induce disturbances in the UMD's pose, potentially leading to motion obstruction in narrow regions, as shown in Fig. 1(a). Such attitude disturbances may lead to deviations of the helical UMD from its intended trajectory (as shown by the green line in Fig. 1(b) toward the blood clot), resulting in dynamic variations in the magnetic gradient force that may pose a risk of vascular damage. Therefore, evaluating the maximum magnetic gradient force acting on the UMD under worst-case conditions is crucial for developing effective risk mitigation strategies. The worst-case gradient force is defined as the maximum magnetic gradient force acting on the UMD, generated by two synchronized rotating magnetic dipoles, when the dipole moments of both the synchronized rotating magnetic dipoles and the UMD independently span all possible orientations in three-dimensional space.

Corresponding author: Bohuan Lin (e-mail: bohuan.lin@xjtlu.edu.cn).
Digital Object Identifier 10.1109/LMAG.2026.3657287

Permanent-magnet-based actuation systems with open configurations are widely employed to actuate UMDs due to their ability to generate strong magnetic fields and their scalability for in vivo applications [Du 2023, Davy 2025]. However, the magnetic fields generated by such systems are inherently nonuniform, resulting in magnetic gradient forces acting on the UMDs. For UMDs that rely primarily on magnetic torque for actuation [Zhang 2025], magnetic gradient forces may adversely affect the stability and accuracy of their locomotion, making such forces undesirable. To address this issue, researchers have proposed various strategies to minimize the magnetic gradient forces acting on UMDs.

Mahoney [2013] proposed that the unwanted magnetic force from the actuator magnet can be significantly reduced either by rapidly increasing the distance between the magnet and the UMD, or by rotating the actuator magnet at a frequency well above the UMD's step-out threshold. However, these actions may result in a loss of UMD localization or control authority. Furthermore, Mahoney [2012] conducted a comprehensive investigation into strategies for mitigating the adverse effects of gradient forces on UMDs actuated by a single rotating magnetic dipole. The first approach involves proportionally scaling the dimensions of the rotating permanent magnet and the UMD's operating distance, thereby preserving the magnetic field strength and torque while reducing the magnetic gradient force due to the diminished field gradient. The second strategy converts the

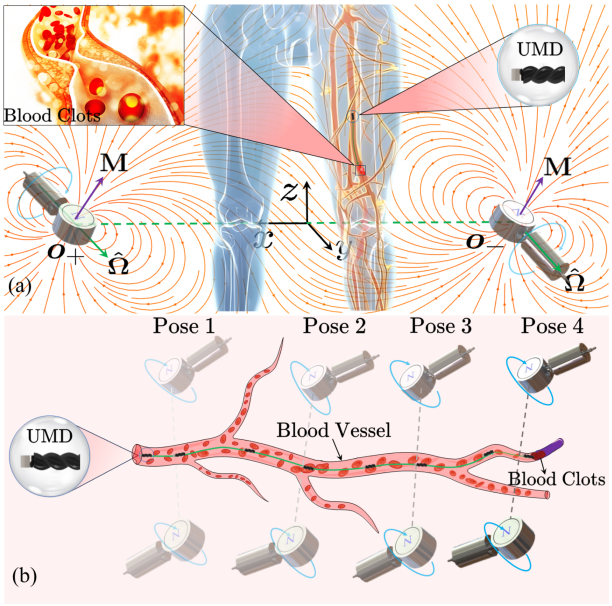

Fig. 1. Helical UMD for the treatment of lower limb thrombosis. (a) UMD is actuated by a rotating magnetic field $\mathbf{B}$, which is generated by two synchronized rotating magnetic dipoles located at positions $\boldsymbol{o}_+$ and $\boldsymbol{o}_-$, respectively. Each dipole possesses a magnetic moment $\mathbf{M}$ and rotates about the axis defined by the unit vector $\hat{\mathbf{\Omega}}$. (b) Real-time adjustment of the posture of two synchronized rotating magnets enables the controlled navigation of the UMD along a vascular path (illustrated by the green line) toward the site of the blood clot. The UMD is subjected to the magnetic gradient force as it moves along intravascular pathways.

gradient force into a lateral force by driving the magnetic dipole along a predefined open-loop trajectory [Mahoney 2011]. The third method establishes an absolute upper bound on the maximum gradient force across all possible UMD dipole orientations for a given dipole rotation axis [Mahoney 2013] and can be extended to evaluate the worst-case gradient force when the UMD is actuated by two synchronized rotating magnetic dipoles. Although magnetic gradient forces at the center of two synchronized dipole fields can be reduced [Hosney 2015], they cannot be fully eliminated.

We separate the magnetic gradient force from hemodynamic effects to determine the worst-case gradient force without considering blood flow. Although this simplification reduces biophysical realism, it is necessary for establishing a conservative upper limit on gradient forces before incorporating full fluid–structure interactions in future studies. In this letter, we present a novel method for evaluating the magnetic gradient force acting on UMDs under worst-case conditions using two synchronized rotating magnetic dipoles.

II. MAGNETIC GRADIENT FORCE

Consider a UMD actuated by two synchronized rotating magnetic dipoles. The UMD consists of a body and a magnet. The body is fabricated using a three-dimensional printer, while the magnet, made of Grade-N45 NdFeB, is mounted at the tail with its magnetic dipole moment oriented perpendicularly to the helix axis of the UMD. As shown in Fig. 2, the two magnetic dipoles are placed at $\boldsymbol{o}_+$ and $\boldsymbol{o}_-$ such that $\boldsymbol{o}_- = -\boldsymbol{o}_+$. Let $\boldsymbol{p}$ be the position of the UMD, and $\boldsymbol{p}_+ = \boldsymbol{p} - \boldsymbol{o}_+$; $\boldsymbol{p}_- = \boldsymbol{p} - \boldsymbol{o}_-$.

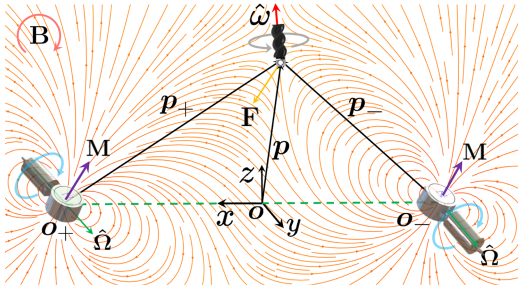

Fig. 2. UMD is subjected to the magnetic gradient force ($\mathbf{F}$) while moving under the influence of a rotating magnetic field generated by two synchronized rotating magnetic dipoles.

Moreover, $\hat{\boldsymbol{p}}_+ = \frac{\boldsymbol{p}_+}{\|\boldsymbol{p}_+\|}$ and $\hat{\boldsymbol{p}}_- = \frac{\boldsymbol{p}_-}{\|\boldsymbol{p}_-\|}$. The magnetic moment ($\mathbf{M}$) of each dipole rotates around the axis $\hat{\mathbf{\Omega}}$ (unit vector of dipole-rotation axis $\mathbf{\Omega}$), causing the magnetic field at UMD position ($\boldsymbol{p}$) to rotate around the axis $\hat{\omega}$ (unit vector of field-rotation axis $\boldsymbol{\omega}$). The gradient force exerted on the UMD under the actuation of two synchronized rotating magnetic dipoles placed at $\boldsymbol{o}_+$ and $\boldsymbol{o}_-$ is given by

$$\mathbf{F} = \mathcal{K}\left(\frac{1}{\|\boldsymbol{p}_+\|^4}\begin{bmatrix}\hat{\mathbf{M}}^{\mathrm{T}}\mathbb{H}_+^x\\ \hat{\mathbf{M}}^{\mathrm{T}}\mathbb{H}_+^y\\ \hat{\mathbf{M}}^{\mathrm{T}}\mathbb{H}_+^z\end{bmatrix} + \frac{1}{\|\boldsymbol{p}_-\|^4}\begin{bmatrix}\hat{\mathbf{M}}^{\mathrm{T}}\mathbb{H}_-^x\\ \hat{\mathbf{M}}^{\mathrm{T}}\mathbb{H}_-^y\\ \hat{\mathbf{M}}^{\mathrm{T}}\mathbb{H}_-^z\end{bmatrix}\right)\hat{\mathbf{m}}$$
$$= \mathcal{K}\mathbb{F}_{\hat{\mathbf{M}}}\hat{\mathbf{m}} \tag{1}$$

where $\mathbf{m}$ is the dipole moment of the UMD, $\hat{\mathbf{m}}$ is the unit vector of $\mathbf{m}$ and $\mathcal{K} = 3\mu_0|\mathbf{m}||\mathbf{M}|/4\pi$, and the matrix $\mathbb{F}_{\hat{\mathbf{M}}}$ is symmetric. Further, matrix $\mathbb{F}_{\hat{\mathbf{M}}}$ depends on $\hat{\mathbf{M}}$, which in fact defines a linear map $\mathbb{G}$: $\mathbb{R}^3 \ni \mathbf{M} \mapsto \mathbb{F}_{\mathbf{M}} \in \mathrm{SyM}_3 \subset \mathbb{R}^{3\times3}$, where SyM_3 is the set of all 3×3 symmetric matrices. The $\mathbb{H}_i^x$ in (1) is the matrix mapping $\hat{\mathbf{M}}$ to magnetic field gradient $\nabla\mathbf{B}$ in the $\bar{\mathbf{x}}$ direction. The $\mathbb{H}_i^x$ is found as

$$\mathbb{H}_i^x = \left(\bar{\mathbf{x}}^{\mathrm{T}}\hat{\boldsymbol{p}}_i\right)\left(\mathbf{I} - 5\hat{\boldsymbol{p}}_i\hat{\boldsymbol{p}}_i^{\mathrm{T}}\right) + \bar{\mathbf{x}}\hat{\boldsymbol{p}}_i^{\mathrm{T}} + \hat{\boldsymbol{p}}_i\bar{\mathbf{x}}^{\mathrm{T}},\ i \in \{+,-\} \tag{2}$$

where matrix $\mathbb{H}_i^x$ are symmetric. The matrices $\mathbb{H}_i^y$ and $\mathbb{H}_i^z$ are determined similarly, and they are purely a function of relative position $\boldsymbol{p}_i$. From (1), we have

$$\mathbb{F}_{\hat{\mathbf{M}}} = \sum_{i=1}^{2}\frac{\left(\hat{\boldsymbol{p}}_i\hat{\mathbf{M}}^{\mathrm{T}} + \hat{\mathbf{M}}\hat{\boldsymbol{p}}_i^{\mathrm{T}}\right)}{\|\boldsymbol{p}_i\|^4} + \sum_{i=1}^{2}\frac{\left(\hat{\mathbf{M}}^{\mathrm{T}}\hat{\boldsymbol{p}}_i\right)\cdot\left(\mathbf{I} - 5\hat{\boldsymbol{p}}_i\hat{\boldsymbol{p}}_i^{\mathrm{T}}\right)}{\|\boldsymbol{p}_i\|^4} \tag{3}$$

from which we observe that $\mathbb{G}$ follows the linearity directly. Further, the trace of $\mathbb{F}_{\hat{\mathbf{M}}}$ can be confirmed to be zero.

We define that the worst-case gradient force $\|\mathbf{F}\|_{\mathrm{worst}}$ as the maximum magnetic gradient force exerted on the UMD when the dipole moments of the two synchronized rotating magnetic dipoles and the dipole moment of the UMD independently sweep through all possible directions in three-dimensional space. For estimating $\|\mathbf{F}\|_{\mathrm{worst}}$, we need to look for the largest possible absolute value of eigenvalues for each $\mathbb{F}_{\hat{\mathbf{M}}}$ and then estimate the maximum magnitude of all these largest possible absolute values as all $\hat{\mathbf{M}} \in S^2$ are taken. In the following, we explain, that for any fixed $\hat{\mathbf{M}} \in S^2$, the largest eigenvalue of the matrix $\mathbb{F}_{\hat{\mathbf{M}}}$ is closely related to its standard norm $\left|\left|\mathbb{F}_{\hat{\mathbf{M}}}\right|\right|_{\mathbb{R}^9}$ in $\mathbb{R}^{3\times3} = \mathbb{R}^9$ (note that $\left|\left|\mathbb{F}_{\hat{\mathbf{M}}}\right|\right|_{\mathbb{R}^9} = \sqrt{\sum_{i,j} a_{ij}^2}$ where a_{ij} is the element of matrix $\mathbb{F}_{\hat{\mathbf{M}}}$), the maximum of which is determined by the largest singular value of the

Algorithm 1: Procedure for Estimating the Upper and Lower Boundaries of $\|\mathbf{F}\|_{\text{worst}}$ Applied to a UMD Under the Influence of two Synchronized Rotating Magnetic Dipoles.

1: Construct the matrix $\mathbb{G}^{\mathrm{T}}\mathbb{G}$ illustrated in (19);
2: Compute the eigenvalues of $\mathbb{G}^{\mathrm{T}}\mathbb{G}$;
3: Find an unit eigenvector $\overline{\mathbf{M}} \in \mathbb{S}^2$ corresponding to the largest eigenvalue of $\mathbb{G}^{\mathrm{T}}\mathbb{G}$;
4: Calculate the eigenvalue of the 3×3 matrix $\mathbb{F}_{\overline{\mathbf{M}}}$ with the largest absolute value $|\bar{\lambda}_{\max}|$;
5: Estimate the magnitude range of $\|\mathbf{F}\|_{\text{worst}}$ using (11);
6: **Output:** The magnitude range of $\|\mathbf{F}\|_{\text{worst}}$.

linear map $\mathbb{G}$. Note that $\mathbb{F}_{\hat{\mathbf{M}}}$ depends on $\hat{\mathbf{M}}$, which in fact defines a linear map $\mathbb{G}$

$$\mathbb{G} : \mathbb{R}^3 \ni \mathbf{M} \mapsto \mathbb{F}_{\mathbf{M}} \in \mathrm{SyM}_3 \tag{4}$$

where SyM_3 is the set of all 3×3 symmetric matrices. The $\mathbb{G}^{\mathrm{T}}\mathbb{G}$ is given in (19); see Appendix A. The adjoint action by $\mathbb{O}(3)$ matrices does not change the stand norm of the symmetric matrices such that

$$\big|\big|\mathrm{C}^{\mathrm{T}}[a_{ij}]\mathrm{C}\big|\big|_{\mathbb{R}^9} = \big|\big|[a_{ij}]\big|\big|_{\mathbb{R}^9} \quad \forall \mathrm{C} \in \mathbb{O}(3). \tag{5}$$

Note that the action also preserves the trace such that $\mathrm{trC}^{\mathrm{T}}[a_{ij}]\mathrm{C} = \mathrm{tr}[a_{ij}]$. Since every element $\mathrm{A} \in \mathrm{SyM}_3$ is related to a diagonal matrix by some $\mathrm{C} \in \mathbb{SO}(3)$

$$\mathrm{C}^{\mathrm{T}}\mathrm{AC} = \begin{bmatrix} \lambda_1 & & \\ & \lambda_2 & \\ & & \lambda_3 \end{bmatrix} \tag{6}$$

with λ_i being its eigenvalues, it holds

$$\big|\big|\mathrm{A}\big|\big|_{\mathbb{R}^9} = \sqrt{\lambda_1^2 + \lambda_2^2 + \lambda_3^2} \tag{7}$$

where the eigenvalues λ_1, λ_2, and λ_3 are relabeled as $\lambda_{\max}$, $\lambda_{\min}$, and λ_{mid} based on the principle of $|\lambda_{\max}| \geq |\lambda_{\mathrm{mid}}| \geq |\lambda_{\min}|$, respectively. For $\mathrm{A} \in \mathrm{SyM}_3^{\mathrm{tr}=0}$, $\mathrm{trA} = \lambda_{\max} + \lambda_{\min} + \lambda_{\mathrm{mid}} = 0$, then $\lambda_{\max}\lambda_{\min} \leq 0$ and $\lambda_{\max}\lambda_{\mathrm{mid}} \leq 0$. Consequently, $\big|\big|\mathrm{A}\big|\big|_{\mathbb{R}^9}^2 = 2|\lambda_{\max}|^2 - 2\lambda_{\mathrm{mid}}\lambda_{\min}$, and then

$$\frac{3}{2}|\lambda_{\max}|^2 \leq \big|\big|\mathrm{A}\big|\big|_{\mathbb{R}^9}^2 \leq 2|\lambda_{\max}|^2 \tag{8}$$

or equivalently

$$\frac{1}{2}\big|\big|\mathrm{A}\big|\big|_{\mathbb{R}^9}^2 \leq |\lambda_{\max}|^2 \leq \frac{2}{3}\big|\big|\mathrm{A}\big|\big|_{\mathbb{R}^9}^2. \tag{9}$$

Define $\|\mathbf{F}\|_{\text{worst}} = \mathcal{K}\|\overline{\mathbf{F}}\|$ where $\|\overline{\mathbf{F}}\|$ is the largest possible absolute value of the eigenvalues of $\mathbb{F}_{\hat{\mathbf{M}}}$ for all $\hat{\mathbf{M}} \in S^2$. Meanwhile, the maximum of $\big|\big|\mathbb{F}_{\overline{\mathbf{M}}}\big|\big|_{\mathbb{R}^9}^2$ is achieved at some $\overline{\mathbf{M}} \in S^2$. The $|\bar{\lambda}_{\max}|$ is denoted by the largest possible absolute value of the eigenvalues of $\mathbb{F}_{\overline{\mathbf{M}}}$. Then

$$\frac{1}{2}\big|\big|\mathbb{F}_{\overline{\mathbf{M}}}\big|\big|_{\mathbb{R}^9}^2 \leq |\bar{\lambda}_{\max}|^2 \leq \|\overline{\mathbf{F}}\|^2 \leq \frac{2}{3}\big|\big|\mathbb{F}_{\overline{\mathbf{M}}}\big|\big|_{\mathbb{R}^9}^2. \tag{10}$$

Then the sharpest estimation for $\|\mathbf{F}\|_{\text{worst}}$ is

$$\|\mathbf{F}\|_{\text{worst}}^{\text{low}} = \mathcal{K}|\bar{\lambda}_{\max}| \leq \|\mathbf{F}\|_{\text{worst}} \leq \sqrt{\frac{2}{3}}\mathcal{K}\big|\big|\mathbb{F}_{\overline{\mathbf{M}}}\big|\big|_{\mathbb{R}^9} = \|\mathbf{F}\|_{\text{worst}}^{\text{up}}. \tag{11}$$

Note that $\big|\big|\mathbb{F}_{\overline{\mathbf{M}}}\big|\big|_{\mathbb{R}^9}^2$ is just the largest eigenvalue of the 3×3 semidefinite matrix $\mathbb{G}^{\mathrm{T}}\mathbb{G}$. Equation (11) provides a way to estimate the magnitude range of $\|\mathbf{F}\|_{\text{worst}}$. Thus, we developed an algorithm to estimate $\|\mathbf{F}\|_{\text{worst}}$, which is presented in Algorithm 1. The magnetic moment values are set as 45.35 for each dipole and $7.5 \times 10^{-4}\mathrm{Am}^2$ for the UMD, based on experimental measurements and theoretical analysis [Mahoney 2012].

Table 1. Estimation of the upper and lower bounds of the magnetic gradient force applied on a UMD under worst-case conditions using two synchronized rotating magnetic dipoles.

(Units of $\|\mathbf{F}\|_{\max}$: μN, $\boldsymbol{p}$: mm)

$\boldsymbol{p}$	$\begin{bmatrix}13.94\\39.95\\-22.05\end{bmatrix}$	$\begin{bmatrix}-0.47\\-49.08\\6.72\end{bmatrix}$	$\begin{bmatrix}-0.81\\21.19\\25.85\end{bmatrix}$	$\begin{bmatrix}9.17\\-20.84\\-30.71\end{bmatrix}$
$\|\mathbf{F}\|_{\text{worst}}$	23.62	19.11	15.17	19.50
$\|\mathbf{F}\|_{\text{worst}}^{\text{low}}$	23.61	18.51	14.77	19.48
$\|\mathbf{F}\|_{\text{worst}}^{\text{up}}$	24.23	21.19	16.72	20.18
$\boldsymbol{p}$	$\begin{bmatrix}28.20\\15.95\\37.95\end{bmatrix}$	$\begin{bmatrix}-10.04\\-4.74\\-36.67\end{bmatrix}$	$\begin{bmatrix}-5.73\\-20.26\\18.63\end{bmatrix}$	$\begin{bmatrix}0.33\\-6.61\\14.93\end{bmatrix}$
$\|\mathbf{F}\|_{\text{worst}}$	34.03	19.91	14.93	8.18
$\|\mathbf{F}\|_{\text{worst}}^{\text{low}}$	34.03	19.90	14.91	7.96
$\|\mathbf{F}\|_{\text{worst}}^{\text{up}}$	34.20	20.54	15.58	9.04
$\boldsymbol{p}$	$\begin{bmatrix}-11.46\\-25.37\\-10.99\end{bmatrix}$	$\begin{bmatrix}-14.67\\-25.28\\-3.35\end{bmatrix}$	$\begin{bmatrix}13.52\\26.64\\-23.22\end{bmatrix}$	$\begin{bmatrix}-5.03\\41.95\\5.08\end{bmatrix}$
$\|\mathbf{F}\|_{\text{worst}}$	18.21	19.91	21.52	18.98
$\|\mathbf{F}\|_{\text{worst}}^{\text{low}}$	18.21	19.93	21.53	18.83
$\|\mathbf{F}\|_{\text{worst}}^{\text{up}}$	18.53	20.11	21.95	20.16
$\boldsymbol{p}$	$\begin{bmatrix}-10.14\\-44.67\\17.59\end{bmatrix}$	$\begin{bmatrix}7.63\\-47.55\\10.62\end{bmatrix}$	$\begin{bmatrix}40.52\\15.94\\-22.72\end{bmatrix}$	$\begin{bmatrix}6.91\\-49.23\\-2.45\end{bmatrix}$
$\|\mathbf{F}\|_{\text{worst}}$	22.09	21.16	51.15	20.97
$\|\mathbf{F}\|_{\text{worst}}^{\text{low}}$	22.04	21.06	51.18	20.85
$\|\mathbf{F}\|_{\text{worst}}^{\text{up}}$	22.95	22.23	51.20	22.13

Table 1 presents the upper and lower bounds of the $\|\mathbf{F}\|_{\text{worst}}$ and compares them to the accurate values obtained with the Monte Carlo simulation. The values are computed at various spatial positions $\boldsymbol{p}$, as shown in Fig. 2, represented as vectors relative to the origin. Note that the positions $\boldsymbol{p}$ reported in Table 1 correspond exactly to those illustrated in Fig. 3. Note that forces during microvascular motion for UMDs with diameters of 1–2 μm are generally kept below 150 μN to prevent vascular damage [Ergeneman 2011].

The results in the table verify our method, and it holds $\|\mathbf{F}\|_{\text{worst}}^{\text{low}} \leq \|\mathbf{F}\|_{\text{worst}} \leq \|\mathbf{F}\|_{\text{worst}}^{\text{up}}$ at all but two the field points $\boldsymbol{p}(-14.67, -25.28, -3.35)$ and $\boldsymbol{p}(13.52, 26.64, -23.22)$. At these exceptional points, the values of $\|\mathbf{F}\|_{\text{worst}}^{\text{low}}$ are a bit larger than the Monte Carlo results of $\|\mathbf{F}\|_{\text{worst}}$, and this in fact testifies our theory instead of denying it. This is because $\|\mathbf{F}\|_{\text{worst}}^{\text{low}}$ is taken to be $\mathcal{K}\bar{\lambda}_{\max}$, which is an actual value of $\|\mathbf{F}\|$, and at certain locations, $\mathcal{K}\bar{\lambda}_{\max}$ is exactly the worst, i.e., $\|\mathbf{F}\|_{\text{worst}} = \mathcal{K}\bar{\lambda}_{\max} = \|\mathbf{F}\|_{\text{worst}}^{\text{low}}$. The computation of $\mathcal{K}\bar{\lambda}_{\max} = \|\mathbf{F}\|_{\text{worst}}$ by solving the eigenvalues of $\mathbb{F}_{\overline{\mathbf{M}}}$ should have returned more accurate results than the Monte Carlo simulation for $\|\mathbf{F}\|_{\text{worst}}^{\text{low}}$, resulting in the seemly discrepancy at these points.

III. MONTE CARLO SIMULATION EXPERIMENT

To validate the effectiveness of the algorithm, we selected 16 positions for the UMD and fixed the two synchronized rotating magnetic dipoles at positions $\boldsymbol{x}_1 = [175\ 0\ 0]$ mm and $\boldsymbol{x}_2 = [-175\ 0\ 0]$ mm, as shown in Fig. 2. These positions were randomly sampled within a spherical region centered at the origin with a radius of 50 mm, as the UMD is most likely to be controlled to swim within this space. We then simultaneously and randomly varied the orientations of the dipole

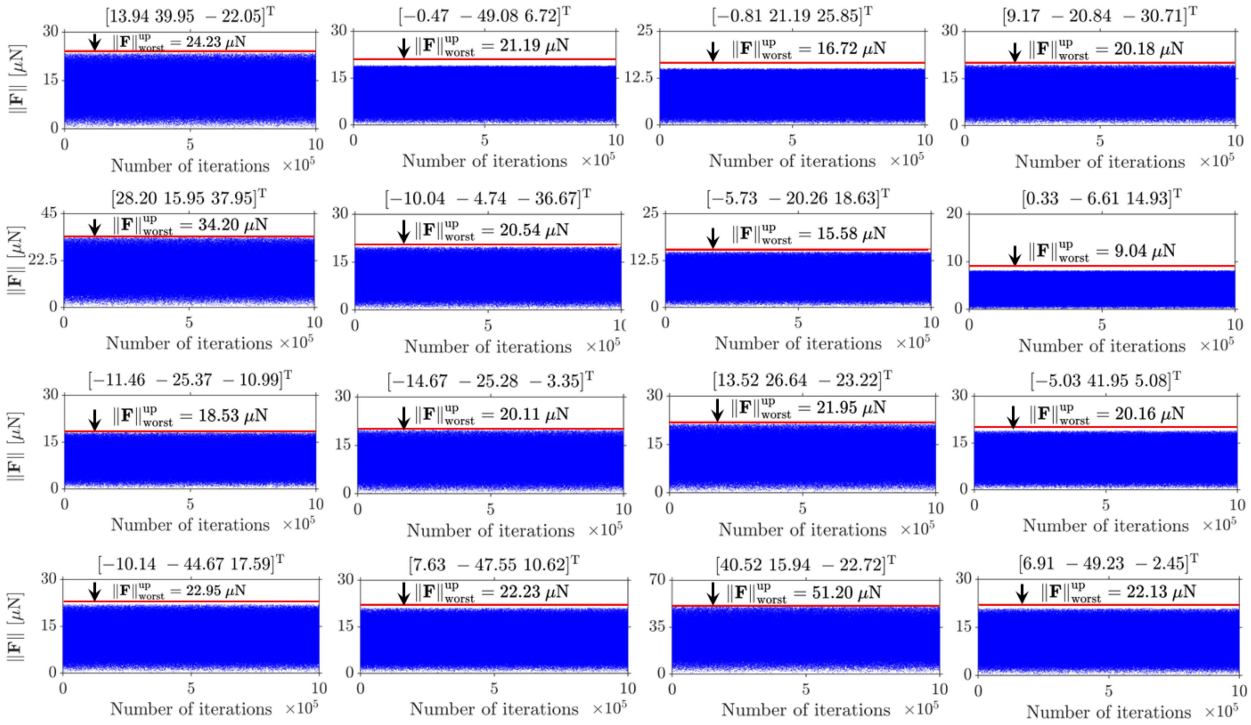

Fig. 3. Monte Carlo-based evaluation of the magnitude of the magnetic gradient force at various spatial positions of the UMD, with the two synchronized rotating magnetic dipoles located at positions $\boldsymbol{x}_1 = [175\ 0\ 0]$ mm and $\boldsymbol{x}_2 = [-175\ 0\ 0]$ mm, respectively. The red line in each subfigure represents the worst-case gradient force at each UMD position.

moments of both the external dipoles and the UMD 1 000 000 times in three-dimensional space. This procedure simulated potential variations in the orientations of the external synchronized rotating dipoles and the UMD within vascular environments.

Fig. 3 illustrates the results of Monte Carlo simulation experiments conducted to estimate the magnitude of the magnetic gradient force, $\|\mathbf{F}\|$, acting on the UMD at various spatial positions $\boldsymbol{p}$ under all possible actuation conditions using two synchronized rotating magnetic dipoles. Each subplot corresponds to a specific spatial location $\boldsymbol{p}$ (in millimeters), and presents the distribution of $\|\mathbf{F}\|$ values over 1 000 000 random iterations. In each subplot, the red horizontal line represents the upper bound $\|\mathbf{F}\|^{\text{up}}_{\text{worst}}$ previously estimated in Table 1, while the blue dots denote the simulated force magnitudes. For all cases, $\|\mathbf{F}\|_{\text{worst}}$ presented in Table 1 was found by Monte Carlo simulation experiments. The results confirm that all simulated values remain below the analytically estimated upper bound, validating the conservative nature of the theoretical force limits.

We observed that most simulated values lie between the analytical upper and lower bounds, with a small portion falling below the lower bound. This is possible, as the analytical lower bound corresponds to a realizable magnetic gradient force generated by a specific configuration of $\mathbf{M}$ and $\mathbf{m}$. Notably, the lower bound may also represent the worst-case gradient force. This analysis statistically validates the force safety margin and supports the use of worst-case estimation for safe UMD trajectory planning in vascular environments.

IV. CONCLUSION

In this letter, we present a novel method for estimating the upper and lower bounds of the magnetic gradient force exerted on a UMD under worst-case conditions, with actuation provided by two synchronized rotating magnetic dipoles. The force safety margin is validated through Monte Carlo simulations, demonstrating the reliability of worst-case estimations in enabling safe UMD navigation within vascular environments, particularly in scenarios where strict control of the applied gradient force is critical to minimizing the risk of vascular damage.

A limitation of the algorithm lies in its conservativeness at certain spatial positions, where the estimated upper bound of the magnetic gradient force under worst-case conditions significantly overestimates the actual force. Future work will aim to refine the algorithm to achieve tighter upper bound estimations that better approximate the true force distribution.

APPENDIX A
EXPRESSION OF THE MATRIX $\mathbb{G}^{\mathrm{T}}\mathbb{G}$

From (3), we can therefore deduce that

$$\mathbb{F}_{\mathbf{M}} = \mathbf{M}\mathbf{P}^{\mathrm{T}} + \mathbf{P}\mathbf{M}^{\mathrm{T}} + \sum_{i=1}^{2} \left(\mathbf{M}\cdot\hat{\boldsymbol{p}}_i\right) \frac{\mathbf{I} - 5\hat{\boldsymbol{p}}_i\hat{\boldsymbol{p}}_i^{\mathrm{T}}}{\|\boldsymbol{p}_i\|^4} \tag{12}$$

where $\boldsymbol{p}_i = \boldsymbol{p} - \boldsymbol{p}_i$ and $\hat{\boldsymbol{p}}_i = \frac{\boldsymbol{p}_i}{\|\boldsymbol{p}_i\|}$, and $\mathbf{P} = \sum_{i=1}^{2} \frac{\hat{\boldsymbol{p}}_i}{\|\boldsymbol{p}_i\|^4}$. $\mathrm{tr}\mathbb{F}^3_{\mathbf{M}}$ from (12). For simplicity, we adopt the notation

$$[\mathbf{M} * \mathbf{P}] = \mathbf{M}\mathbf{P}^{\mathrm{T}} + \mathbf{P}\mathbf{M}^{\mathrm{T}} \tag{13}$$

and

$$\mathbf{P}_{\mathbf{M}} = \sum_{i=i}^{2} \left(\mathbf{M}\cdot\hat{\boldsymbol{p}}_i\right) \frac{\hat{\boldsymbol{p}}_i\hat{\boldsymbol{p}}_i^{\mathrm{T}}}{\|\boldsymbol{p}_i\|^4}. \tag{14}$$

Therefore, $\mathbb{F}_{\mathbf{M}}$ can be described as

$$\mathbb{F}_{\mathbf{M}} = [\mathbf{M} * \mathbf{P}] - 5\mathbf{P}_{\mathbf{M}} + (\mathbf{M}\cdot\mathbf{P})\,\mathbf{I} = \mathbf{A}_{\mathbf{M}} + (\mathbf{M}\cdot\mathbf{P})\,\mathbf{I}. \tag{15}$$

Note that $\mathrm{tr}\mathbb{F}_{\mathbf{M}} = 0$ and $\mathbf{A}_{\mathbf{M}} = \mathbb{F}_{\mathbf{M}} - (\mathbf{M}\cdot\mathbf{P})\mathbf{I}$, and then

$$\begin{aligned}\mathrm{tr}\mathbb{F}_{\mathbf{M}}^2 &= \mathrm{tr}\left[\mathbb{F}_{\mathbf{M}}\mathbf{A}_{\mathbf{M}}\right] + (\mathbf{M}\cdot\mathbf{P})\cdot\mathrm{tr}\mathbb{F}_{\mathbf{M}}\\ &= \mathrm{tr}\mathbf{A}_{\mathbf{M}}^2 + (\mathbf{M}\cdot\mathbf{P})\cdot\mathrm{tr}\mathbf{A}_{\mathbf{M}}\\ &= \mathrm{tr}\mathbf{A}_{\mathbf{M}}^2 + (\mathbf{M}\cdot\mathbf{P})\cdot\mathrm{tr}\left[\mathbb{F}_{\mathbf{M}} - (\mathbf{M}\cdot\mathbf{P})\,\mathbf{I}\right]\\ &= \mathrm{tr}\mathbf{A}_{\mathbf{M}}^2 - 3\,(\mathbf{M}\cdot\mathbf{P})^2\,.\end{aligned} \tag{16}$$

Now, it remains to calculate $\mathrm{tr}\mathbf{A}_{\mathbf{M}}^2$

$$\begin{aligned}\mathrm{tr}\mathbf{A}_{\mathbf{M}}^2 &= \mathrm{tr}[\mathbf{M}*\mathbf{P}]^2 + 25\mathrm{tr}\mathbf{P}_{\mathbf{M}}^2 - 5[\mathbf{M}*\mathbf{P}]\mathbf{P}_{\mathbf{M}} - 5\mathbf{P}_{\mathbf{M}}[\mathbf{M}*\mathbf{P}]\\ &= 2\,(\mathbf{M}\cdot\mathbf{P})^2 + 2\|\mathbf{P}\|^2 + \sum_{i=1}^{2}\left(\frac{5}{\|\boldsymbol{p}_i\|^8} - \frac{20(\hat{\boldsymbol{p}}_1\cdot\hat{\boldsymbol{p}}_2)}{\|\boldsymbol{p}_1\|^4\|\boldsymbol{p}_2\|^4}\right)\left(\mathbf{M}\cdot\hat{\boldsymbol{p}}_i\right)^2\\ &\quad + \frac{50(\hat{\boldsymbol{p}}_1\cdot\hat{\boldsymbol{p}}_2)^2}{\|\boldsymbol{p}_1\|^4\|\boldsymbol{p}_2\|^4}\left(\mathbf{M}\cdot\hat{\boldsymbol{p}}_1\right)\left(\mathbf{M}\cdot\hat{\boldsymbol{p}}_2\right).\end{aligned} \tag{17}$$

As a result, it holds for any $\mathbf{M}\in\mathbb{R}^3$. Note that $\mathbb{G}$ is a matrix expressed in (4). Thus, we have

$$\begin{aligned}\mathbf{M}^{\mathrm{T}}\left[\mathbb{G}^{\mathrm{T}}\mathbb{G}\right]\mathbf{M} &= \mathrm{tr}\mathbb{F}_{\mathbf{M}}^2\\ &= \mathbf{M}^{\mathrm{T}}\Big[2\|\mathbf{P}\|^2\mathbf{I} - \mathbf{P}\mathbf{P}^{\mathrm{T}}\\ &\quad + \sum_{i=1}^{2}\left(\frac{5}{\|\boldsymbol{p}_i\|^8} - \frac{20(\hat{\boldsymbol{p}}_1\cdot\hat{\boldsymbol{p}}_2)}{\|\boldsymbol{p}_1\|^4\|\boldsymbol{p}_2\|^4}\right)\hat{\boldsymbol{p}}_i\hat{\boldsymbol{p}}_i^{\mathrm{T}}\\ &\quad + \frac{25(\hat{\boldsymbol{p}}_1\cdot\hat{\boldsymbol{p}}_2)^2}{\|\boldsymbol{p}_1\|^4\|\boldsymbol{p}_2\|^4}\left[\hat{\boldsymbol{p}}_1\hat{\boldsymbol{p}}_2^{\mathrm{T}} + \hat{\boldsymbol{p}}_2\hat{\boldsymbol{p}}_1^{\mathrm{T}}\right]\Big]\mathbf{M}\end{aligned} \tag{18}$$

which implies

$$\begin{aligned}\mathbb{G}^{\mathrm{T}}\mathbb{G} &= 2\|\mathbf{P}\|^2\mathbf{I} - \mathbf{P}\mathbf{P}^{\mathrm{T}} + \sum_{i=1}^{2}\left(\frac{5}{\|\boldsymbol{p}_i\|^8} - \frac{20(\hat{\boldsymbol{p}}_1\cdot\hat{\boldsymbol{p}}_2)}{\|\boldsymbol{p}_1\|^4\|\boldsymbol{p}_2\|^4}\right)\hat{\boldsymbol{p}}_i\hat{\boldsymbol{p}}_i^{\mathrm{T}}\\ &\quad + \frac{25(\hat{\boldsymbol{p}}_1\cdot\hat{\boldsymbol{p}}_2)^2}{\|\boldsymbol{p}_1\|^4\|\boldsymbol{p}_2\|^4}\left[\hat{\boldsymbol{p}}_1\hat{\boldsymbol{p}}_2^{\mathrm{T}} + \hat{\boldsymbol{p}}_2\hat{\boldsymbol{p}}_1^{\mathrm{T}}\right].\end{aligned} \tag{19}$$

ACKNOWLEDGMENT

This work was supported in part by the European Research Council under the European Union's Horizon 2020 Research, Innovation program through the MAESTRO project under Grant 866494, in part by the Research development Fund of Xi'an Jiaotong Liverpool University under Grant RDF-24-01-086, in part by the Wenzhou Municipal Key Science and Research Program under Grant ZG2023023, in part by the Wenling Municipal Key Science and Research Program under Grant 2023G00009, in part by the Wenzhou Science and Technology Major Project under Grant ZG2024005, and in part by the Natural Science Foundation of Zhejiang province under Grant LQN25E050031.

REFERENCES

Bishop J J, Popel A S, Intaglietta M, Johnson P C (2001), "Rheological effects of red blood cell aggregation in the venous network: A review of recent studies," *Biorheol.*, vol. 38, pp. 263–274, doi: 10.1177/0006355X2001038002003003.

Davy J, Brockdorff M, Valdastri P (2025), "Utilizing field gradient measurements for object tracking in permanent magnet based manipulation systems," *IEEE Trans. Magn.*, vol. 61, 8001005, doi: 10.1109/TMAG.2025.1234567.

Du X, Yu J (2023), "Image-integrated magnetic actuation systems for localization and remote actuation of medical miniature robots: A survey," *IEEE Trans. Robot.*, vol. 39, pp. 2549–2568, doi: 10.1109/TRO.2023.3263340.

Ergeneman O, Pokki J, Počepcová V, Hall H, Abbott J J, Nelson B J (2011), "Characterization of puncture forces for retinal vein cannulation," *J. Med. Devices–Trans. ASME*, vol. 5, 044504, doi: 10.1115/1.4005318.

Hosney A, Klingner A, Misra S, Khalil I S M (2015), "Propulsion and steering of helical magnetic microrobots using two synchronized rotating dipole fields in three-dimensional space," in *Proc. 2015 IEEE/RSJ Int. Conf. Intell. Robots Syst.*, pp. 1988–1993, doi: 10.1109/IROS.2015.7353612.

Khalil I S M, Adel A, Mahdy D, Micheal M M, Mansour M, Hamdi N, Misra S (2019), "Magnetic localization and control of helical robots for clearing superficial blood clots," *APL Bioeng.*, vol. 3, 026104, doi: 10.1063/1.5090872.

Mahoney A W, Abbott J J (2014), "Generating rotating magnetic fields with a single permanent magnet for propulsion of untethered magnetic devices in a lumen," *IEEE Trans. Robot.*, vol. 30, pp. 411–420, doi: 10.1109/TRO.2013.2238561.

Mahoney A W, Cowan D L, Miller K M, Abbott J J (2012), "Control of untethered magnetically actuated tools using a rotating permanent magnet in any position," in *Proc. 2012 IEEE Int. Conf. Robot. Autom.*, pp. 3375–3380, doi: 10.1109/ICRA.2012.6225175.

Mahoney A W, Abbott J J (2011), "Managing magnetic force applied to a magnetic device by a rotating dipole field," *Appl. Phys. Lett.*, vol. 99, 134103, doi: 10.1063/1.3630674.

Mahoney A W, Wright S E, Abbott J J (2013), "Managing the attractive magnetic force between an untethered magnetically actuated tool and a rotating permanent magnet," in *Proc. 2013 IEEE Int. Conf. Robot. Autom.*, pp. 5366–5371, doi: 10.1109/ICRA.2013.6631294.

Song Y, Ou J, Miao J, Zhang X, Jiang J, Tian H, Peng F, Tu Y (2024), "Magnetically powered microrobotic swarm for integrated mechanical/photothermal/photodynamic thrombolysis," *Small*, vol. 20, 2403440, doi: 10.1002/smll.202403440.

Zhang Z, Klingner A, Misra S, Khalil I S M (2025), "Design and control of a permanent magnet-based robotic system for navigating tetherless magnetic devices in viscous environments," *Sci. Rep.*, vol. 15, 31041, doi: 10.1038/s41598-025-15247-7.